Computers and Geotechnics 38 (2011) 375–382

Contents lists available at ScienceDirect

Computers and Geotechnics

journal homepage: www.elsevier.com/locate/compgeo

Numerical modeling of cyclic mobility based on fuzzy-set concepts in plasticity theory

Yu Bao [a], Stein Sture [b,*]

[a] Department of Civil Engineering Technology, Environmental Management and Safety, Rochester Institute of Technology, CST-3151, 78 Lomb Memorial Drive, Rochester, NY 14623-5603, USA
[b] Regent Hall, 26 UCB, University of Colorado at Boulder, CO 80309-026, USA

ARTICLE INFO

Article history:
Received 2 April 2010
Received in revised form 3 January 2011
Accepted 7 January 2011

Keywords:
Cyclic mobility
Fuzzy-set plasticity
Soil dilatancy
Constitutive modeling

ABSTRACT

In this paper, the application of an efficient, transparent and accurate kinematic-cyclic constitutive model based on the fuzzy-set concepts and incremental plasticity theory is presented to show its capability in modeling cyclic mobility of saturated granular soil. The nature and kinematic mechanism of the membership functions in the fuzzy-set constitutive model are illustrated. The model's capability of modeling soil dilatancy is investigated. Important features of volume change and pore water pressure build-up related to soil cyclic mobility are captured. The formulation of the proposed model is relatively simple and it can be readily implemented in finite element codes. The enhanced fuzzy-set model is capable of simulating ground motion problems particularly related to cyclic mobility, soil liquefaction, and spreading behavior.

1. Introduction

Strong ground motion induces a tendency for soil skeleton volume change, which causes progressive pore water pressure build-up and significant loss of soil strength. Pressure dependency and shear induced dilatancy are important characteristics for accurate prediction of sandy soil behavior under cyclic loading [4–,9,11,18,20,22,24,25].

Fuzzy-set plasticity theory was first proposed by Klisinski et al. [14]. In this paper, an enhanced kinematic and cyclic plasticity model based on the concept of fuzzy-set plasticity was proposed to simulate realistic sand behavior during unloading and reloading cycles. The enhanced model is not only able to capture the general nonlinear behavior of soil, but also essential soil characteristics, such as confinement dependency, soil skeleton contraction and dilation, critical state soil mechanics features and pore pressure build-up. More importantly, the proposed model involves relatively simple and explicit formulations.

Fuzzy-set plasticity borrows the term "fuzzy-set" from probability theory, but it does not consider related to probability analysis. In fuzzy-set plasticity, it is assumed that there exists an ultimate yield surface, where the behavior of the material is entirely plastic [12]. In addition, the material behavior inside the initial yield surface is purely elastic. The elasto-plastic response between the initial and the ultimate yield surfaces is characterized by a fuzzy set as shown in Fig. 1. The main difference between the formulation of fuzzy-set plasticity theory and that of the classical plasticity theory is that the elasto-plastic response between the initial and the ultimate yield surfaces is not characterized in the conventional sense but by a fuzzy set. Instead of determining the plastic modulus from the consistency condition, the plastic modulus is defined in terms of the value of a membership function $\gamma(\boldsymbol{\sigma}) \in (0, 1)$, such that $\gamma = 1$ for the purely elastic behavior, whereas $\gamma = 0$ when the stress point is on the ultimate yield surface. The scalar $\gamma(\boldsymbol{\sigma})$ represents the membership degree that the stress $\boldsymbol{\sigma}$ is close to the set of stresses representing purely elastic behavior [12–14].

In classical elastoplasticity with a single plastic mechanism, the volumetric–deviatoric coupling emerges as a consequence of the assumed plastic potential. On the other hand, the proposed fuzzy-set model adopts two independent plastic mechanisms and gives the tensorial incremental stress–strain relation for all components, and deals with deviatoric–volumetric coupling in a consistent manner, and therefore predict pore water pressure in a rational way.

2. Model formulations

The stress controlled incremental stress–strain formulation is straightforward and can be readily implemented. The explicit expression of the stress control stress–strain formulation for the fuzzy-set model in the p–q space was given in Ref. [2].

* Corresponding author.
E-mail addresses: axbite@rit.edu (Y. Bao), stein.sture@colorado.edu (S. Sture).

0266-352X/$ - see front matter © 2011 Elsevier Ltd. All rights reserved.
doi:10.1016/j.compgeo.2011.01.001

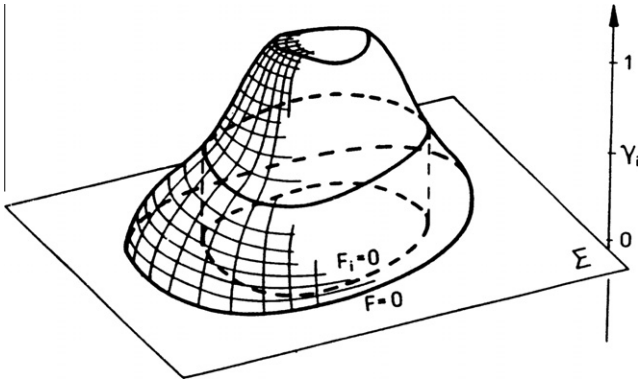

Fig. 1. "Fuzzy" yield surface specified by a given constant value of the membership function [14].

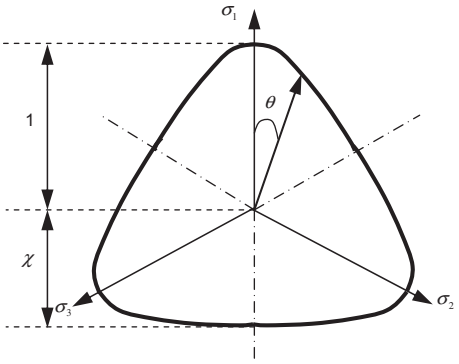

Fig. 2. Lode's angle in deviatoric plane [23].

$$d\boldsymbol{\varepsilon} = \mathbf{C}^{ep} d\boldsymbol{\sigma} = \left(\begin{bmatrix} \frac{1}{K} & 0 \\ 0 & \frac{1}{3G} \end{bmatrix} + \frac{1}{H_d} \frac{1}{a_1^2 + g^2(\theta)} \begin{bmatrix} a_1^2 & -a_1 g(\theta) B \\ 0 & g^2(\theta) \end{bmatrix} + \frac{1}{H_v} \begin{bmatrix} 1 & 0 \\ 0 & 0 \end{bmatrix} \right) \begin{Bmatrix} dp \\ dq \end{Bmatrix} \tag{1}$$

where p and q denote confining pressure and deviatoric stress, respectively. $H_d = \left(H_d^* + \frac{M_d \cdot \gamma_d^{s_d}}{1-\gamma_d^{s_d+1}} \right) \left(\frac{p}{p_0} \right)^{n_p}$, is the deviatoric plastic modulus, which is related to the effective confinement; $\gamma_d \in [0,1]$ is the deviatoric membership function; H_d^* is the hardening modulus; $H_v = \left(\frac{M_v \cdot \gamma_v^{s_v}}{1-\gamma_v^{s_v+1}} \right) \left(\frac{p}{p_0} \right)^{n_p}$, is the volumetric plastic modulus, in which $\gamma_v \in [0,1]$ is the volumetric membership function. The parameter B is the dilatancy parameter, which determines the soil dilatancy behavior [2].

The formulation in Cartesian space is preferred in order to implement the model into a finite element code.

$$d\boldsymbol{\varepsilon} = d\boldsymbol{\varepsilon}^e + d\boldsymbol{\varepsilon}^p = d\boldsymbol{\varepsilon}^e + d\boldsymbol{\varepsilon}_d^p + d\boldsymbol{\varepsilon}_v^p = \begin{Bmatrix} d\varepsilon_x \\ d\varepsilon_y \\ d\varepsilon_z \\ d\gamma_{xy} \\ d\gamma_{yz} \\ d\gamma_{zx} \end{Bmatrix} \tag{2}$$

where the elastic strain can be expressed as,

$$d\boldsymbol{\varepsilon}^e = \mathbf{C}^e d\boldsymbol{\sigma} = \begin{bmatrix} \frac{3K+G}{9KG} & -\frac{3K-2G}{18KG} & -\frac{3K-2G}{18KG} & 0 & 0 & 0 \\ -\frac{3K-2G}{18KG} & \frac{3K+G}{9KG} & -\frac{3K-2G}{18KG} & 0 & 0 & 0 \\ -\frac{3K-2G}{18KG} & -\frac{3K-2G}{18KG} & \frac{3K+G}{9KG} & 0 & 0 & 0 \\ 0 & 0 & 0 & \frac{1}{G} & 0 & 0 \\ 0 & 0 & 0 & 0 & \frac{1}{G} & 0 \\ 0 & 0 & 0 & 0 & 0 & \frac{1}{G} \end{bmatrix} \begin{Bmatrix} d\sigma_x \\ d\sigma_y \\ d\sigma_z \\ d\tau_{xy} \\ d\tau_{yz} \\ d\tau_{zx} \end{Bmatrix} \tag{3}$$

and the deviatoric strain increment can be written as,

$$d\boldsymbol{\varepsilon}_d^p = \mathbf{C}_d^p d\boldsymbol{\sigma} = \frac{1}{H_d} \mathbf{m}_d \mathbf{n}_d^T d\boldsymbol{\sigma} \tag{4}$$

The deviatoric ultimate yield surface can be described as

$$\begin{aligned} F_d &= g(\theta) q - a_0 - a_1 p \\ &= g(\theta) \sqrt{\sigma_x^2 + \sigma_y^2 + \sigma_z^2 - \sigma_x\sigma_y - \sigma_y\sigma_z - \sigma_z\sigma_x + 3\tau_{xy}^2 + 3\tau_{yz}^2 + 3\tau_{zx}^2} \\ &\quad - a_0 - \frac{a_1}{3}(\sigma_x + \sigma_y + \sigma_z) \end{aligned} \tag{5}$$

where $p = \frac{1}{3}(\sigma_x + \sigma_y + \sigma_z)$, $q = \sqrt{\sigma_x^2 + \sigma_y^2 + \sigma_z^2 - \sigma_x\sigma_y - \sigma_y\sigma_z - \sigma_z\sigma_x + 3\tau_{xy}^2 + 3\tau_{yz}^2 + 3\tau_{zx}^2}$, $a_1 = M_c + \kappa\langle -\psi \rangle$, a_0 is a material constant, and θ is the Lode angle [23] as illustrated in Fig. 2. The "elliptical" function $g(\theta)$ determines the shape of the trace of the ultimate yield surface in any deviatoric plane.

$$g(\theta) = \frac{4(1-\chi^2)\cos^2(\theta - \frac{\pi}{3}) + (2\chi - 1)^2}{2(1-\chi^2)\cos(\theta - \frac{\pi}{3}) + (2\chi - 1)\sqrt{4(1-\chi^2)\cos^2(\theta - \frac{\pi}{3}) + 5\chi^2 - 4\chi}} \tag{6}$$

The state parameter ψ is defined as the difference between the current void ratio and the critical void ratio, i.e. $\psi = e - e_c$. For a loose soil, $\psi > 0$; and for a dense soil, $\psi < 0$.

Experimental evidence shows that the critical void ratio e_c depends on the mean effective stress as follows [17,1].

$$e_c = e_{ref} - c_\lambda \cdot \ln \frac{p}{p_{ref}}$$

Assuming that $\varepsilon_v^e \approx 0$, plastic volumetric strain is related to the void ratio e as follows.

$$\begin{aligned} \varepsilon_v^p &\approx \varepsilon_v = \frac{\Delta V}{V_o} = \frac{-\Delta e}{1+e_0} = \frac{e_0 - e}{1+e_0} \\ d\varepsilon_v^p &= d\varepsilon_v = -\frac{de}{1+e_0} \end{aligned} \tag{7}$$

For loose soil, $e > e_c$, $-\psi < 0$, $\kappa\langle -\psi \rangle = 0$

$$a_1 = M_c \tag{8}$$

$$H_d^* = -\frac{\partial F_d}{\partial a_1} \frac{\partial a_1}{\partial \psi} \frac{\partial \psi}{\partial \varepsilon_v^p} \frac{\partial \varepsilon_v^p}{\partial \varepsilon_{vd}^p} \frac{\partial F_d}{\partial p} = 0 \tag{9}$$

For dense soil, $e < e_c$, $-\psi > 0$, $\kappa\langle -\psi \rangle = -\psi$

$$\begin{aligned} &a_1 = M_c - \kappa \cdot \psi \\ &\psi = e - e_c = e_0 - (1+e_0)\varepsilon_v^p - e_c \\ &\Rightarrow a_1 = M_c - \kappa[e_0 - (1+e_0)\varepsilon_v^p - e_c] \end{aligned} \tag{10}$$

$$\begin{aligned} H_d^* &= -\frac{\partial F_d}{\partial a_1} \frac{\partial a_1}{\partial \psi} \frac{\partial \psi}{\partial \varepsilon_v^p} \frac{\partial \varepsilon_v^p}{\partial \varepsilon_{vd}^p} \frac{\partial F_d}{\partial p} \\ H_d^* &= -(-p)(-\kappa)[-(1+e_0)]1(-a_1) = -p\kappa \cdot (1+e_0) a_1 \\ &= -\frac{\sigma_x + \sigma_y + \sigma_z}{3} \cdot \kappa \cdot (1+e_0) a_1 \end{aligned} \tag{11}$$

Eq. (10) shows that the model is capable of capturing the gradual softening behavior of dense sands due to homogeneous dilation, since the slope of the strength envelope decreases with the void ratio.

The normal of the deviatoric yield surface can be described as,

$$\mathbf{n}_d = \frac{1}{\sqrt{\left(\frac{\partial F_d}{\partial \sigma_x}\right)^2 + \left(\frac{\partial F_d}{\partial \sigma_y}\right)^2 + \left(\frac{\partial F_d}{\partial \sigma_z}\right)^2 + \left(\frac{\partial F_d}{\partial \tau_{xy}}\right)^2 + \left(\frac{\partial F_d}{\partial \tau_{yz}}\right)^2 + \left(\frac{\partial F_d}{\partial \tau_{zx}}\right)^2}} \begin{Bmatrix} \frac{\partial F_d}{\partial \sigma_x} \\ \frac{\partial F_d}{\partial \sigma_y} \\ \frac{\partial F_d}{\partial \sigma_z} \\ \frac{\partial F_d}{\partial \tau_{xy}} \\ \frac{\partial F_d}{\partial \tau_{yz}} \\ \frac{\partial F_d}{\partial \tau_{zx}} \end{Bmatrix} \tag{12}$$

and direction of the strain increment is,

$$\mathbf{m}_d = \mathbf{T}\mathbf{n}_d$$

where the dilatancy matrix can be defined as,

$$\mathbf{T} = \begin{bmatrix} \frac{1}{3}(B+2) & \frac{1}{3}(B+2) & \frac{1}{3}(B+2) & 0 & 0 & 0 \\ \frac{1}{3}(B+2) & \frac{1}{3}(B+2) & \frac{1}{3}(B+2) & 0 & 0 & 0 \\ \frac{1}{3}(B+2) & \frac{1}{3}(B+2) & \frac{1}{3}(B+2) & 0 & 0 & 0 \\ 0 & 0 & 0 & 1 & 0 & 0 \\ 0 & 0 & 0 & 0 & 1 & 0 \\ 0 & 0 & 0 & 0 & 0 & 1 \end{bmatrix} \tag{13}$$

The Phase Transformation Surface (PTS) is the collection of stress points at which the volumetric changes of dense or medium sandy soil transform from contraction to dilation [9,25,26].

The effective stress ratio is defined as

$$\eta = \frac{q}{p} = \frac{\sigma_x + \sigma_y + \sigma_z}{3\sqrt{\sigma_x^2 + \sigma_y^2 + \sigma_z^2 - \sigma_x\sigma_y - \sigma_y\sigma_z - \sigma_z\sigma_x + 3\tau_{xy}^2 + 3\tau_{yz}^2 + 3\tau_{zx}^2}} \tag{14}$$

On PTS, $\eta = \eta_{PT}$, no volumetric change takes place; below PTS, $\eta < \eta_{PT}$, contraction takes place; and above PTS, $\eta > \eta_{PT}$, dilation takes place.

In the fuzzy-set model, the volumetric change is controlled by the model dilatancy parameter "B". An exponential expression for "B" was proposed as [2].

Loading and reloading:

$$\text{Below PTS}: \quad B = \alpha_1|\psi|\left[\exp\left(1 - \frac{|\eta|}{|\eta_{PT}|}\right) - 1\right] \tag{15}$$

$$\text{Above PTS}: \quad B = \alpha_2|\psi|\left[\exp\left(\frac{|\eta| - |\eta_{PT}|}{|\eta_F| - |\eta_{PT}|}\right) - 1\right] \tag{16}$$

Unloading:

$$B = \beta|\psi|\exp\left(\frac{|\eta|}{|\eta_F|}\right) \tag{17}$$

where α_1, α_2 and β are model parameters, and η_F is the effective stress ratio at material failure.

The volumetric strain increment can be described as,

$$d\boldsymbol{\varepsilon}_v^p = \mathbf{C}_v^p d\boldsymbol{\sigma} = \frac{1}{H_v}\mathbf{n}_v\mathbf{n}_v^T d\boldsymbol{\sigma} \tag{18}$$

The yield function for the volumetric part can be simplified as a cap along the confining stress axis,

$$F_v = p - p_e = \frac{1}{3}(\sigma_x + \sigma_y + \sigma_z) - p_e \tag{19}$$

The normal of the volumetric yield surface can be described as,

$$\mathbf{n}_v = \frac{1}{\sqrt{\left(\frac{\partial F_v}{\partial \sigma_x}\right)^2 + \left(\frac{\partial F_v}{\partial \sigma_y}\right)^2 + \left(\frac{\partial F_v}{\partial \sigma_z}\right)^2 + 0 + 0 + 0}} \begin{Bmatrix} \frac{\partial F_v}{\partial \sigma_x} \\ \frac{\partial F_v}{\partial \sigma_y} \\ \frac{\partial F_v}{\partial \sigma_z} \\ 0 \\ 0 \\ 0 \end{Bmatrix} = \frac{1}{\sqrt{3}} \begin{Bmatrix} 1 \\ 1 \\ 1 \\ 0 \\ 0 \\ 0 \end{Bmatrix} \tag{20}$$

Although the stress control formulation is straightforward and readily implemented at the material level, it has the following disadvantages:

(1) It causes numerical instability near the peak stress point.
(2) It is unable to capture the post peak behavior of softening materials.
(3) It is awkward to implement in standard finite element displacement-based schemes.

The strain-control formulation has the advantages of being able to resolve the above mentioned issues.

$$d\boldsymbol{\sigma} = \mathbf{D}^e d\boldsymbol{\varepsilon}^e = \mathbf{D}^e(d\boldsymbol{\varepsilon} - d\boldsymbol{\varepsilon}_d - d\boldsymbol{\varepsilon}_v) \tag{21}$$

$$d\boldsymbol{\varepsilon}_d = \dot{\lambda}_d \mathbf{m}_d \tag{22}$$

$$d\boldsymbol{\varepsilon}_v = \dot{\lambda}_v \mathbf{m}_v \tag{23}$$

where the plastic multiplier $\dot{\lambda}$ can be expressed as:

$$\dot{\lambda} = \frac{1}{H}\dot{\mu} = \frac{1}{H}\mathbf{n} \cdot d\boldsymbol{\sigma}$$

Substituting (22) and (23) into (21), yields

$$d\boldsymbol{\sigma} = \mathbf{D}^e d\boldsymbol{\varepsilon}^e = \mathbf{D}^e(d\boldsymbol{\varepsilon} - \dot{\lambda}_d \mathbf{m}_d - \dot{\lambda}_v \mathbf{m}_v) \tag{24}$$

$$\mathbf{D}^e = \begin{bmatrix} K + \frac{4}{3}G & K - \frac{2}{3}G & K - \frac{2}{3}G & 0 & 0 & 0 \\ K - \frac{2}{3}G & K + \frac{4}{3}G & K - \frac{2}{3}G & 0 & 0 & 0 \\ K - \frac{2}{3}G & K - \frac{2}{3}G & K + \frac{4}{3}G & 0 & 0 & 0 \\ 0 & 0 & 0 & G & 0 & 0 \\ 0 & 0 & 0 & 0 & G & 0 \\ 0 & 0 & 0 & 0 & 0 & G \end{bmatrix} \tag{25}$$

Using the consistency condition equations for the deviatoric and volumetric loading surface, respectively,

$$dF = \frac{\partial F}{\partial \boldsymbol{\sigma}} \cdot d\boldsymbol{\sigma} + \frac{\partial F}{\partial \gamma} d\gamma = \mathbf{n} \cdot d\boldsymbol{\sigma} - \dot{\mu} = 0$$

where $\dot{\mu} = -\frac{\partial F}{\partial \gamma} d\gamma$, which is used to determine the loading–unloading conditions:

$$\begin{cases} \dot{\mu} > 0, \quad dF = 0 & \text{plastic loading;} \\ \dot{\mu} = 0, \quad dF = 0 & \text{neutral loading;} \\ \dot{\mu} < 0, \quad dF = 0, & \text{elastic loading} \end{cases}$$

we obtain the following,

$$\begin{cases} dF_d = \mathbf{n}_d \cdot [\mathbf{D}^e(d\boldsymbol{\varepsilon} - \dot{\lambda}_d \mathbf{m}_d - \dot{\lambda}_v \mathbf{m}_v)] - H_d \dot{\lambda}_d = 0 \\ dF_v = \mathbf{n}_v \cdot [\mathbf{D}^e(d\boldsymbol{\varepsilon} - \dot{\lambda}_d \mathbf{m}_d - \dot{\lambda}_v \mathbf{m}_v)] - H_v \dot{\lambda}_v = 0 \end{cases} \tag{26}$$

By rearranging the terms in the above simultaneous Eq. (26), we get the following matrix form,

$$\begin{bmatrix} H_d + \mathbf{n}_d \cdot (\mathbf{D}^e \mathbf{m}_d) & \mathbf{n}_d \cdot (\mathbf{D}^e \mathbf{m}_v) \\ \mathbf{n}_v \cdot (\mathbf{D}^e \mathbf{m}_d) & H_v + \mathbf{n}_v \cdot (\mathbf{D}^e \mathbf{m}_v) \end{bmatrix} \begin{Bmatrix} \dot{\lambda}_d \\ \dot{\lambda}_v \end{Bmatrix} = \begin{Bmatrix} \mathbf{n}_d \cdot (\mathbf{D}^e d\boldsymbol{\varepsilon}) \\ \mathbf{n}_v \cdot (\mathbf{D}^e d\boldsymbol{\varepsilon}) \end{Bmatrix} \tag{27}$$

and then the deviatoric and volumetric multipliers can be obtained by solving (27) for $\dot{\lambda}_d$ and $\dot{\lambda}_v$,

$$\dot{\lambda}_d = \frac{[H_v + \mathbf{n}_v \cdot (\mathbf{D}^e \mathbf{m}_v)][\mathbf{n}_d \cdot (\mathbf{D}^e d\boldsymbol{\varepsilon})] - [\mathbf{n}_d \cdot (\mathbf{D}^e \mathbf{m}_v)][\mathbf{n}_v \cdot (\mathbf{D}^e d\boldsymbol{\varepsilon})]}{[H_d + \mathbf{n}_d \cdot (\mathbf{D}^e \mathbf{m}_d)][H_v + \mathbf{n}_v \cdot (\mathbf{D}^e \mathbf{m}_v)] - [\mathbf{n}_d \cdot (\mathbf{D}^e \mathbf{m}_v)][\mathbf{n}_v \cdot (\mathbf{D}^e \mathbf{m}_d)]}$$

$$\Rightarrow \dot{\lambda}_d = \frac{[H_v + \mathbf{n}_v \cdot (\mathbf{D}^e \mathbf{m}_v)]\mathbf{n}_d - [\mathbf{n}_d \cdot (\mathbf{D}^e \mathbf{m}_v)]\mathbf{n}_v}{[H_d + \mathbf{n}_d \cdot (\mathbf{D}^e \mathbf{m}_d)][H_v + \mathbf{n}_v \cdot (\mathbf{D}^e \mathbf{m}_v)] - [\mathbf{n}_d \cdot (\mathbf{D}^e \mathbf{m}_v)][\mathbf{n}_v \cdot (\mathbf{D}^e \mathbf{m}_d)]} \cdot (\mathbf{D}^e d\boldsymbol{\varepsilon}) = \mathbf{A}_d \cdot (\mathbf{D}^e d\boldsymbol{\varepsilon}) \tag{28}$$

$$\dot{\lambda}_v = \frac{[H_d + \mathbf{n}_d \cdot (\mathbf{D}^e \mathbf{m}_d)][\mathbf{n}_v \cdot (\mathbf{D}^e d\boldsymbol{\varepsilon})] - [\mathbf{n}_v \cdot (\mathbf{D}^e \mathbf{m}_d)][\mathbf{n}_d \cdot (\mathbf{D}^e d\boldsymbol{\varepsilon})]}{[H_d + \mathbf{n}_d \cdot (\mathbf{D}^e \mathbf{m}_d)][H_v + \mathbf{n}_v \cdot (\mathbf{D}^e \mathbf{m}_v)] - [\mathbf{n}_d \cdot (\mathbf{D}^e \mathbf{m}_v)][\mathbf{n}_v \cdot (\mathbf{D}^e \mathbf{m}_d)]}$$

$$\Rightarrow \dot{\lambda}_v = \frac{[H_d + \mathbf{n}_d \cdot (\mathbf{D}^e \mathbf{m}_v)]\mathbf{n}_v - [\mathbf{n}_v \cdot (\mathbf{D}^e \mathbf{m}_d)]\mathbf{n}_d}{[H_d + \mathbf{n}_d \cdot (\mathbf{D}^e \mathbf{m}_d)][H_v + \mathbf{n}_v \cdot (\mathbf{D}^e \mathbf{m}_v)] - [\mathbf{n}_d \cdot (\mathbf{D}^e \mathbf{m}_v)][\mathbf{n}_v \cdot (\mathbf{D}^e \mathbf{m}_d)]} \cdot (\mathbf{D}^e d\boldsymbol{\varepsilon}) = \mathbf{A}_v \cdot (\mathbf{D}^e d\boldsymbol{\varepsilon}) \tag{29}$$

By substituting (28) and (29) into (24), we obtain

$$d\boldsymbol{\sigma} = [\mathbf{D}^e - (\mathbf{D}^e \mathbf{m}_d)(\mathbf{D}^e \mathbf{A}_d)^T - (\mathbf{D}^e \mathbf{m}_v)(\mathbf{D}^e \mathbf{A}_v)^T] d\boldsymbol{\varepsilon} = \mathbf{D}^{ep} d\boldsymbol{\varepsilon} \tag{30}$$

where

$$\mathbf{D}^{ep} = \mathbf{D}^e - (\mathbf{D}^e \mathbf{m}_d)(\mathbf{D}^e \mathbf{A}_d)^T - (\mathbf{D}^e \mathbf{m}_v)(\mathbf{D}^e \mathbf{A}_v)^T \tag{31}$$

2.1. Kinematic mechanism of deviatoric membership function γ_d

The value of the deviatoric membership function γ_d is related to the effective stress ratio η. Consider the ultimate yield function $F_d = g(\theta)q - a_0 - a_1 p = 0$, and for most sands, $a_0 = 0$, and therefore, the yielding surface can be simplified as

$$q = \frac{a_1}{g(\theta)} p = \eta_F p \tag{32}$$

where $\eta_F = \frac{a_1}{g(\theta)}$ is the effective stress ratio at failure. Note that η_F is not a constant, but varies with the state parameter and loading path.

Let γ_{d0} and γ_{dF} be the values of the deviatoric membership function at $\eta = 0$ and $\eta = \eta_F$ in initial loading, respectively.

Under cyclic loading conditions, we use the memory of the maximum effective stress ratio. The schematic illustrations of the kinematic mechanism of the deviatoric membership function are shown in Figs. 3 and 4a–c (assuming $g(\theta) = 1$, $\gamma_{d0} = 1$ and $\gamma_{dF} = 0$).

(1) From "a" to "b", initial loading to the "+q" direction
(2) From "b" to "c", unloading from the "+q" direction and reloading to the "−q" direction
(3) From "c" to "d", unloading from the "−q" direction and reloading to the "+q" direction

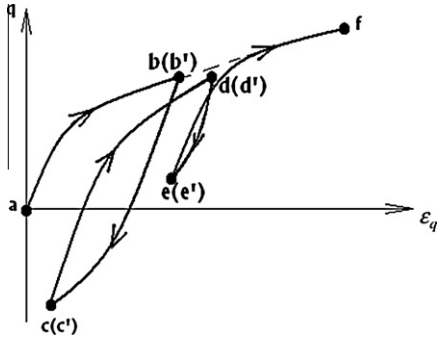

Fig. 3. Deviatoric stress–strain response curve for two loading cycles.

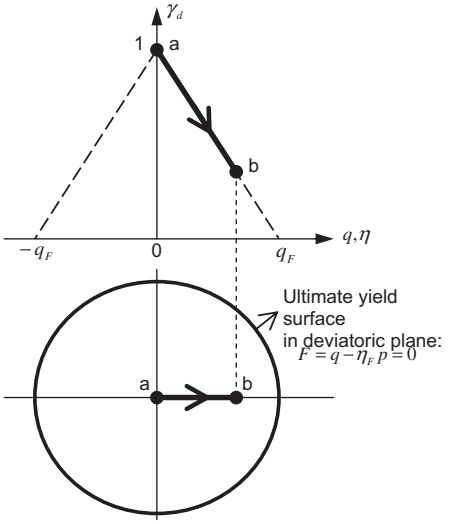

Fig. 4a. Pictorial illustration of kinematic mechanism of deviatoric membership function γ_d from Point "a" to Point "b".

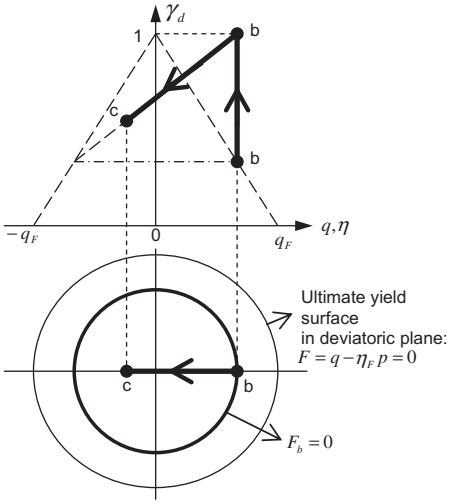

Fig. 4b. Pictorial illustration of kinematic mechanism of deviatoric membership function γ_d from Point "b" to Point "c".

The values of the deviatoric membership function can be calculated in terms of the effective stress ratio based on loading conditions,

Monotonic Loading:

$$\gamma_d = \gamma_{d0} - \frac{|\eta|}{|\eta_F|}(\gamma_{d0} - \gamma_{dF}) \tag{33}$$

Unloading: record the maximum effective stress ratio $\eta_{\max}$ and the corresponding value of membership function $\gamma_{d\eta_{\max}}$.

If $\eta_{i+1} < \eta_i$ and $|\eta_{i+1}| < |\eta_{\max}|$:

$$\gamma_d = \gamma_{d0} - \frac{\eta_{\max} - \eta_{i+1}}{2\eta_{\max}}(\gamma_{d0} - \gamma_{d\eta_{\max}}) \tag{34}$$

and update $\eta_{\min} = \eta_{i+1}$

If $\eta_{i+1} < \eta_i$ and $|\eta_{i+1}| \geqslant |\eta_{\max}|$:

$$\gamma_d = \gamma_{d0} - \frac{|\eta_{i+1}|}{|\eta_F|}(\gamma_{d0} - \gamma_{dF}) \tag{35}$$

and update $\eta_{\min} = \eta_{i+1}$ and $\eta_{\max} = |\eta_{i+1}|$

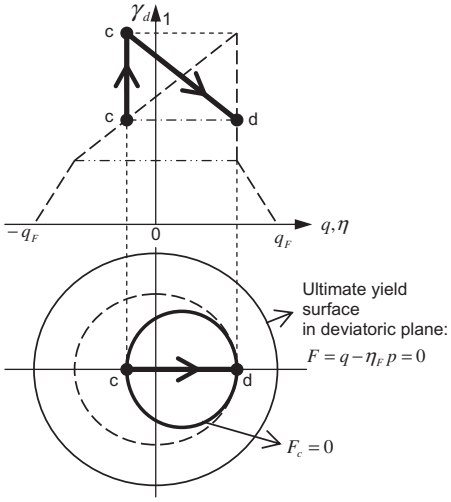

Fig. 4c. Pictorial illustration of kinematic mechanism of deviatoric membership function γ_d from Point "c" to Point "d".

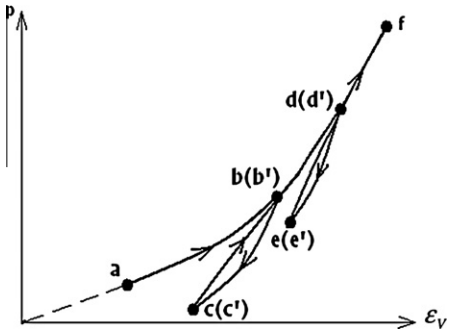

Fig. 5. Mean stress–strain response curve for two loading cycles.

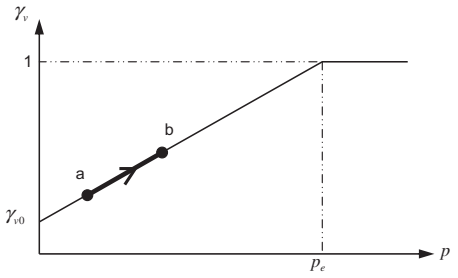

Fig. 6a. Concept illustration of kinematic mechanism of volumetric membership function γ_v from Point "a" to Point "b".

Reloading: record the minimum effective stress ratio $\eta_{\min}$, the corresponding value of the membership function $\gamma_{d\eta_{\min}}$, and the maximum absolute value of $|\eta_{\max}|$.

If $\eta_{i+1} > \eta_i$ and $|\eta_{i+1}| < |\eta_{\max}|$:

$$\gamma_d = \gamma_{d0} - \frac{\eta_{i+1} - \eta_{\min}}{\eta_{\max} - \eta_{\min}}(\gamma_{d0} - \gamma_{d\eta_{\min}}) \tag{36}$$

If $\eta_{i+1} \geqslant \eta_i$ and $|\eta_{i+1}| \geqslant |\eta_{\max}|$:

$$\gamma_d = \gamma_{d0} - \frac{|\eta|}{|\eta_F|}(\gamma_{d0} - \gamma_{dF}) \tag{37}$$

and update $\eta_{\max} = \eta_{i+1}$

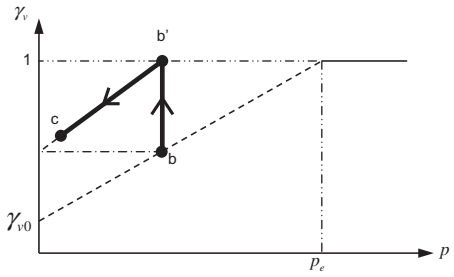

Fig. 6b. Concept illustration of kinematic mechanism of volumetric membership function γ_v from Point "b" to Point "c".

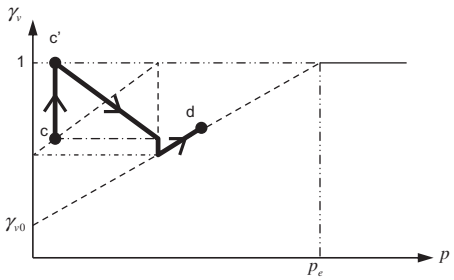

Fig. 6c. Concept illustration of kinematic mechanism of volumetric membership function γ_v from Point "c" to Point "d".

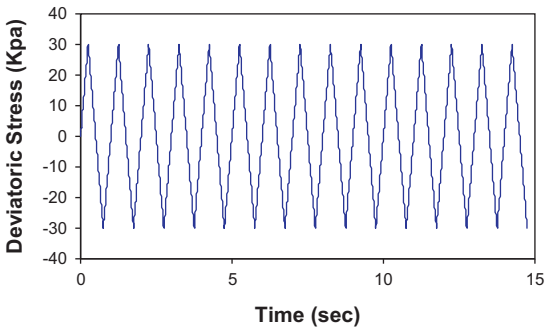

Fig. 7. Loading history of deviatoric stress.

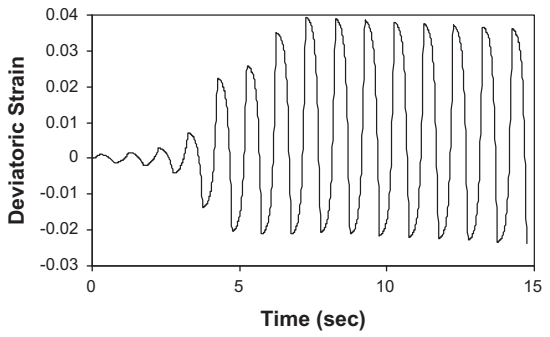

Fig. 8a. Deviatoric strain history.

2.2. Kinematic mechanism of volumetric membership function γ_v

The volumetric membership function γ_v depends on the mean effective stress p. The memory of the maximum effective stress

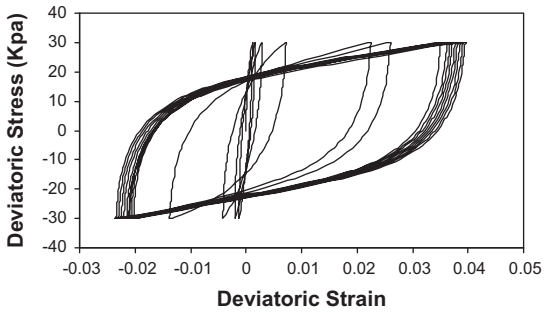

Fig. 8b. Deviatoric stress–deviatoric strain cyclic response.

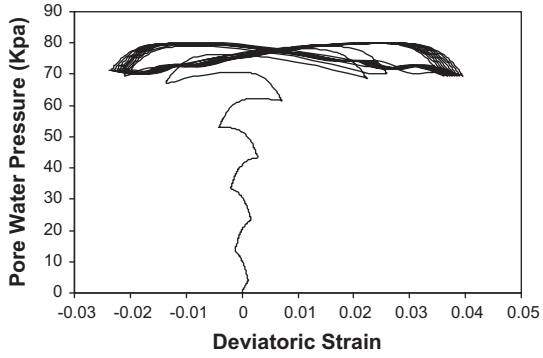

Fig. 8c. Pore water pressure–deviatoric strain cyclic response.

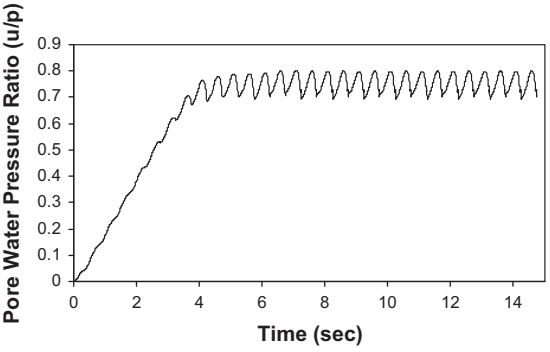

Fig. 8d. Pore water pressure build-up history.

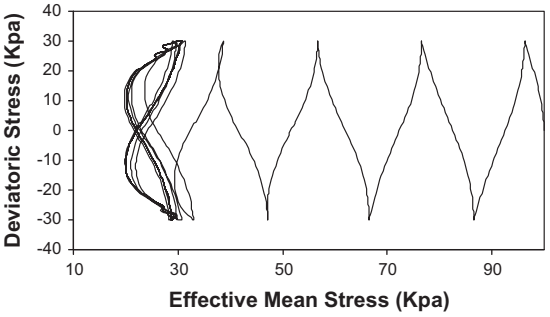

Fig. 8e. Effective stress path approaching liquefaction.

ratio is adopted to characterize the volumetric membership function under cyclic loading. The schematic illustrations of the kinematic mechanism of the volumetric membership function are shown in Figs. 5 and 6a–c.

Table 1
Fuzzy-set model parameters.

Fuzzy-set parameters	Reference bulk modulus K_0 (kPa)	13,831
	Reference shear modulus G_0 (kPa)	5028
	Reference mean pressure p_0 (kPa)	100
	Pressure dependence coefficient n_p	0.5
	Locking mean pressure p_e (kPa)	12,657
	Deviatoric plastic modulus coefficient M_d (kPa)	387,000
	Deviatoric plastic modulus coefficient s_d	2.1415
	Locking plastic modulus coefficient M_l (kPa)	160,100
	Locking plastic modulus coefficient s_l	1.6472
	Deviatoric failure membership function γ_{dF}	0.10
	Locking membership at the mean pressure of "0" γ_{l0}	0.25
Critical state parameters	Initial void ratio e_0	0.776
	Reference void ratio e_{ref}	0.650
	Slope of the void ratio critical line c_λ	0.01
	Failure envelop coefficient κ	1
	Angle of failure line φ_F (°)	35
	Angle of phase transformation line φ_{PT} (°)	30
Dilatancy parameters	Contraction parameter under loading α_1	−15
	Dilation parameter under loading α_2	13
	Contraction parameter under unloading β	28

Table 2
Dilatancy parameters.

Dilatancy parameters	α_1	α_2	β
Curve 1	−15	13	28
Curve 2	−7.5	6.5	14

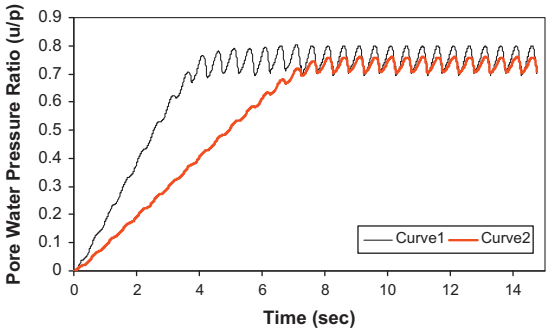

Fig. 9. Effect of change of dilatancy parameters on pore water pressure buildup.

(1) From "a" to "b", initial loading
(2) From "b" to "c", unloading
(3) From "c" to "d", reloading

The volumetric membership function can be calculated in terms of the mean effective stress based on the following loading conditions:

Under monotonic loading conditions, the following relationship holds,

$$\gamma_v = \gamma_{v0} + \frac{p}{p_e}(1 - \gamma_{v0}) \tag{38}$$

Unloading: In this case it is necessary to maintain records of the maximum mean effective stress $p_{\max}$ and the $\gamma_{vp\max}$, and then update $p_{\min}$ and the $\gamma_{vp\min}$

$$\gamma_v = 1 - \frac{p_{\max} - p}{p_{\max}}(1 - \gamma_{vp\max}) \tag{39}$$

Reloading: Record the minimum mean stress $p_{\min}$ and the corresponding value of the membership function $\gamma_{vp\min}$.

If $p < p_{\max}$,

$$\gamma_v = 1 - \frac{p - p_{\min}}{p_{\max} - p_{\min}}(1 - \gamma_{vp\min}) \tag{40}$$

If $p > p_{\max}$,

$$\gamma_v = \gamma_{v0} + \frac{p}{p_e}(1 - \gamma_{v0}) \text{ and update } p_{\max} \text{ and the } \gamma_{vp\max} \tag{41}$$

3. Model capabilities: modeling cyclic mobility

The model capabilities are focused on deviatoric–volumetric strain coupling under cyclic loading, particularly under undrained condition, which is the predominant loading condition leading to liquefaction. The modeling of volumetric changes are mostly of a densification type resulting in a pore water pressure increase, which reduces the soil strength and elastic stiffness moduli. Soil skeleton volumetric changes depend on the loading history.

3.1. Example 1

Undrained cyclic shear loading, the total mean stress keeps constant of 100 kPa and the deviatoric stress increases gradually from 0 to 30 kPa, unloads to 0, and reloads to 30 kPa, and the amplitude of deviatoric stress keeps constant for 15 cycles. The loading history is shown in Fig. 7 and the model responses are shown in Fig. 8a–e. Model parameters are listed in Table 1.

The model responses are consistent with a large number of undrained laboratory experiments, which have been used to study the cyclic behavior of sands [3,10,15,16,19,21,26]:

(1) The deviatoric strain history in Fig. 8a shows that the deviatoric strain amplitude increases with the number of loading cycles and tends to reach a steady value.
(2) The cyclic deviatoric stress–strain curves, as shown in Fig. 8b describe a cycle-by-cycle degradation in strength.
(3) Pore water pressure build-up is directly related to the volume change of soil skeleton. Fig. 8c shows that the volume change of soil skeleton increases cycle-by-cycle and tends to approach a steady state value.
(4) The enhanced fuzzy-set model successfully captures the features of progressive pore water pressure build-up and cyclic pore water pressure variations under cyclic shear loading, as shown in Fig. 8d.
(5) As shown in Fig. 8e, under undrained conditions, the dilatancy induced volume increase leads to an immediate reduction in pore water pressure and associated increase in effective confinement. The model response verifies that the enhanced fuzzy set is capable of modeling soil shear dilatancy accurately.

The modeling capability of dilatancy behavior is governed by the dilatancy parameters in the enhanced fuzzy-set model. The following example demonstrates the effect of dilatancy parameter change on the behavior of pore water pressure build-up.

3.2. Example 2

The values of the dilatancy parameters of the two comparison curves are listed in Table 2, and other fuzzy-set model parameters are the same as those listed in Table 1. The pore pressure generation curves with different dilatancy parameters are illustrated in Fig. 9.

Pore water pressure build-up history is of great interest to understand the mechanism of cyclic mobility and soil liquefaction. The effects of dilatancy parameters on pore water pressure build-up patterns are investigated using the fuzzy-set model. In Fig. 9, Curve 1 is the reference response that uses the same model parameters as shown in Example 1, and Curve 2 displays the result of pore pressure generation using the dilatancy parameters decreased by one half. The model responses verify that the proposed dilatancy parameters in the enhanced fuzzy-set model control the soil skeleton dilatancy behavior and the pore water pressure build-up pattern. By comparing Curve 1 with Curve 2, we can conclude that higher values of dilatancy parameters will result in faster pore water pressure build-up; higher peak value of pore water pressure and larger amplitude of cyclic pore water pressure variations.

4. Conclusions

Based on fundamental mechanics principles and fuzzy set elasto-plasticity theory, a kinematic and cyclic plasticity model has been implemented to simulate realistic sand behavior including dilatancy and cyclic mobility. Explicit stress–strain relationships for both stress control and strain-control formulations were developed. For the enhanced fuzzy-set model, the plastic moduli are determined in terms of the membership functions of fuzzy sets rather than by the classic plasticity theory. New dilatancy parameters were adopted to accurately simulate soil dilatancy under cyclic shear loading. The proposed formulation of the model is relatively simple and it is readily implemented into a finite element code.

The enhanced fuzzy-set model is numerically robust and shows good performance in modeling soil skeleton dilatancy features under cyclic loading. From the proposed model formulation and model responses, it can be concluded that:

(1) The enhanced fuzzy-set model is capable of modeling hysteresis loops of soils subjected to cyclic loading.
(2) The enhanced fuzzy-set model is capable of simulating soil strength degradation under cyclic loading.
(3) The model is able to trace the soil skeleton volumetric changes by introducing the soil dilatancy parameters.
(4) The model can successfully capture the features of cyclic pore water pressure build-up under undrained conditions, which helps to understand the mechanism of soil liquefaction during earthquakes.

References

[1] Bao Y, Ge Y-N, Sture S. Unconstrained optimization and calibration of a kinematic-cyclic plasticity model. ASCE geotechnical special publication no. 128, Soil constitutive models – evaluation, selection, and calibration, GeoFrontiers, 2005, Austin, Texas; 2005. p. 45–68.
[2] Bao Y, Ge Y-N, Sture S, Ko H-Y. Numerical modeling of cyclic mobility in saturated soil. In: Proceedings of 3rd biot conference on poromechanics, Norman, Oklahoma; 2005. p. 353–9.
[3] Castro G. Liquefaction and cyclic mobility of saturated sands. J Geotech Eng, ASCE 1975;101(GT6):551–69.
[4] Castro G, Poulos SJ. Factors affecting liquefaction and cyclic mobility. J Geotech Eng, ASCE 1977;103(GT6):501–16.
[5] Dafalias YF, Popov E. Plastic internal variables formalism of cyclic plasticity. J Appl Mech 1976;98(4):645–51.
[6] Dafalias YF, Herrmann LR. Bounding surface formulation of soil plasticity. In: Pande G, Zienkiewicz OC, editors. Soil mechanics – transient and cyclic loads. London: John Wiley and Sons, Inc; 1982. p. 253–82.
[7] Dafalias YF, Herrmann LR. Bounding surface plasticity II: application to isotropic cohesive soils. J Eng Mech 1986;112(12):1263–91.
[8] Dafalias YF, Manzari MT. Simple plasticity sand model accounting for fabric change effects. J Eng Mech 2004;130(6):622–34.

[9] Elgamal A, Yang Z, Parra E, Ragheb A. Modeling of cyclic mobility in saturated cohesionless soils. Int J Plast 2003;19(6):883–905.
[10] Ishihara K, Verdugo R, Acacio A. Characterization of cyclic behavior of sand and post-seismic stability analyses. In: Proceedings of IX Asian regional conference on soil mechanics and foundation engineering, Bangkok, Thailand; 1991.
[11] Ishihara K. Liquefaction and flow failure during earthquakes. Geotechnique 1993;43(3):351–415.
[12] Klisinski M. Plasticity theory based on fuzzy sets. J Eng Mech, ASCE 1988;114(4):563–82.
[13] Klisinski M, Abifadel N, Runesson K, Sture S. Modeling of the behavior of dry sand by an elasto-plastic 'fuzzy set' model. Comput Geotech 1991;11:229–61.
[14] Klisinski M, Alawi MM, Sture S, Ko H-Y, Muir Wood D. Elasto-plastic model for sand based on fuzzy sets. International workshop on constitutive equations for granular non-cohesive soils. Case Western Reserve University; 1987.
[15] Koga Y, Matsuo O. Shaking table tests of embankments resting on liquefiable sandy ground. Soils Found 1990;30(4):162–74.
[16] Krstelj I, Prevost JH. Dynamic effects in a saturated layered soil deposit: centrifuge modeling. Soil Dynam Earthquake Eng 1992;11:485–96.
[17] Li XS, Dafalias YF, Wang ZL. State-dependant dilatancy in critical-state constitutive modelling of sand. Can Geotech J 1999;36(4):599–611.
[18] Prevost JH. A simple plasticity theory for frictional cohesionless soils. Soil Dynam Earthquake Eng 1985;4(1):9–17.
[19] Seed HB, Lee KL. Liquefaction of saturated sands during cyclic loading. J Soil Mech Found Div, ASCE 1966;92(SM6):105–34.
[20] Seed HB. Evaluation of soil liquefaction effects on level ground during earthquakes. Liquefaction problems in geotechnical engineering, 1-104, ASCE Annual convention and exposition, Philadelphia, PA; 1976.
[21] Seed HB. Soil liquefaction and cyclic mobility evaluation for level ground during earthquakes. J Geotech Eng Div, ASCE 1979;105(GT2):201–55.
[22] Sture S, Mould JC, Ko HY. Elastic–plastic anisotropic hardening constitutive model and prediction of behavior for dry quartz sand. Constitutive relations for soil. In: Gudehus G, Darve F, Vardoulakis I, editors. Results of the international workshop on constitutive relations for soils, Grenoble. A.A. Balkema; 1982. p. 227–48.
[23] Willam KJ, Warnke EP. Constitutive model for the triaxial behavior of concrete. Seminar on concrete structures subjected to triaxial stresses. ISMES, Bergamo, Italy, 1974, Published in IABSE Report 19, Zurich, III-I; 1975.
[24] Yang Z, Elgamal A. Application of unconstrained optimization and sensitivity analysis to calibration of a soil constitutive model. Int J Numer Anal Methods Geomech 2003;27:1277–97.
[25] Yang Z, Elgamal A, Parra E. A computational model for liquefaction and associated shear deformation. J Geotech Geoenviron Eng 2003;129(12):1119–27.
[26] Zhang JM, Shamoto Y, Tokimatsu K. Moving critical and phase transformation stress state lines of saturated sands during undrained cyclic shear. Soils Found 1997;37(2):51–9.